The Astrophysical Journal Letters, 831:L14 (6pp), 2016 November 10 doi:10.3847/2041-8205/831/2/L14

DISCOVERY OF COHERENT PULSATIONS FROM THE ULTRALUMINOUS X-RAY SOURCE NGC 7793 P13

F. Fürst[1], D. J. Walton[1,2], F. A. Harrison[1], D. Stern[2], D. Barret[3], M. Brightman[1], A. C. Fabian[4], B. Grefenstette[1], K. K. Madsen[1], M. J. Middleton[5], J. M. Miller[6], K. Pottschmidt[7,8], A. Ptak[8], V. Rana[1], and N. Webb[3]
[1] Cahill Center for Astronomy and Astrophysics, California Institute of Technology, Pasadena, CA 91125, USA; fuerst@caltech.edu
[2] Jet Propulsion Laboratory, California Institute of Technology, Pasadena, CA 91109, USA
[3] IRAP/CNRS, 9 Av. colonel Roche, BP 44346, F-31028 Toulouse cedex 4, France and Université de Toulouse III Paul Sabatier/OMP, Toulouse, France
[4] Institute of Astronomy, Madingley Road, Cambridge CB3 0HA, UK
[5] Department of Physics and Astronomy, University of Southampton, Highfield, Southampton SO17 1BJ, UK
[6] Department of Astronomy, The University of Michigan, Ann Arbor, MI 48109, USA
[7] CRESST, Department of Physics, and Center for Space Science and Technology, UMBC, Baltimore, MD 21250, USA
[8] NASA Goddard Space Flight Center, Greenbelt, MD 20771, USA
Received 2016 September 22; revised 2016 October 10; accepted 2016 October 15; published 2016 November 3

ABSTRACT

We report the detection of coherent pulsations from the ultraluminous X-ray source (ULX) NGC 7793 P13. The ≈0.42 s nearly sinusoidal pulsations were initially discovered in broadband X-ray observations using *XMM-Newton* and *NuSTAR* taken in 2016. We subsequently also found pulsations in archival *XMM-Newton* data taken in 2013 and 2014. The significant ($\gg 5\sigma$) detection of coherent pulsations demonstrates that the compact object in P13 is a neutron star, and given the observed peak luminosity of $\approx 10^{40}$ erg s^{-1} (assuming isotropy), it is well above the Eddington limit for a 1.4 $M_{\odot}$ accretor. This makes P13 the second ULX known to be powered by an accreting neutron star. The pulse period varies between epochs, with a slow but persistent spin-up over the 2013–2016 period. This spin-up indicates a magnetic field of $B \approx 1.5 \times 10^{12}$ G, typical of many Galactic accreting pulsars. The most likely explanation for the extreme luminosity is a high degree of beaming; however, this is difficult to reconcile with the sinusoidal pulse profile.

Key words: accretion, accretion disks – pulsars: individual (NGC 7793 P13) – stars: neutron – X-rays: binaries

1. INTRODUCTION

Due to their high luminosities ($L > 10^{39}$ erg s^{-1}), most ultraluminous X-ray sources (ULXs) have been thought to harbor black holes (BHs) with masses ranging from $M \approx 10\,M_{\odot}$, consistent with a stellar remnant accreting above the Eddington rate (e.g., Poutanen et al. 2007; Middleton et al. 2015), to intermediate-mass BHs ($M \approx 10^{2-5}\,M_{\odot}$; e.g., Miller et al. 2004) in a sub-Eddington disk accretion regime. The discovery of coherent pulsations in the ULX M82 X-2 showed that the compact object in this system is a neutron star (Bachetti et al. 2014). M82 X-2 reaches X-ray luminosities of 2×10^{40} erg s^{-1}, demonstrating that accreting neutron stars can reach luminosities more than 100 times Eddington (assuming $M_{\rm NS} \approx 1.4\,M_{\odot}$).

Accreting magnetized neutron stars can reach these apparent super-Eddington luminosities through a number of mechanisms. High magnetic fields collimate the accretion flow, allowing material to accrete onto the polar regions while radiation escapes from the sides of the column (Basko & Sunyaev 1976). In addition, large magnetic fields reduce the scattering cross section for electrons (Herold 1979), reducing the radiation pressure and increasing the effective Eddington luminosity. The combination of these effects with the consequent geometric beaming have been used to explain known super-Eddington local sources such as SMC X-1 (e.g., Coe et al. 1981).

A very highly magnetized (magnetar-like) neutron star has been invoked to explain the extreme luminosity of M82 X-2 (e.g., Dall'Osso et al. 2015; Ekşi et al. 2015; Mushtukov et al. 2015). It is difficult, however, to explain the near-sinusoidal pulse profile in the context of a highly beamed system. In contrast, some theoretical work suggests the field in M82 X-2 may be relatively low (10^9 G), based on the ratio of the spin-up rate to the luminosity, which is an order of magnitude lower than typical X-ray pulsars (Kluźniak & Lasota 2015). These authors argue that a disk truncated at a large radius, as would occur for a high *B*-field system, would not provide the required lever arm to power the observed spin-up. The nature of ULX pulsars is very much in question, since no model can explain all the observed characteristics.

The ULX NGC 7793 P13 (hereafter P13; Read & Pietsch 1999) is one the few ULXs with a dynamical mass constraint of the compact object and a well classified optical companion (spectral type B9Ia; Motch et al. 2011). Optical monitoring revealed a ≈64 day photometric period also seen in the radial velocity of the He II emission. Adopting this as the orbital period of the binary system, Motch et al. (2014) derive a dynamical mass estimate for the accretor of 3–15 $M_{\odot}$, assuming a BH. This constraint, together with a peak luminosity of $L_{\rm X} > 6 \times 10^{39}$ erg s^{-1}, makes P13 a prime example for a super-Eddington system.

Here, we report on new *XMM-Newton* (Jansen et al. 2001) and *NuSTAR* (Harrison et al. 2013) X-ray observations of P13 in which we detect coherent pulsations, requiring that P13 hosts a highly super-Eddington neutron star accretor.[9]

2. OBSERVATIONS AND DATA REDUCTION

Following the detection of a high flux with *Swift* (Gehrels et al. 2004), we triggered a coordinated observation with *XMM-Newton* and *NuSTAR* in 2016 May (total exposures of ≈50 and ≈110 ks, respectively). In addition to these new observations,

[9] During preparation of this manuscript, Israel et al. (2016) reported on an independent discovery of this period in archival *XMM-Newton* data. Our study includes newer *XMM-Newton* and *NuSTAR* data that extend the investigation to higher energies and cover a longer time range.

Table 1
Details of the X-Ray Observations of NGC 7793 P13 Considered in This Work

Epoch	Mission(s)	OBSID(s)	Date	$F_{0.3-10}$ (10^{-14} erg cm^{-2} s^{-1})	P (ms)	$\dot{P}$ (10^{-10} s s^{-1})
X1	*XMM-Newton*	0693760101	2012 May 14	$2.0^{+1.7}_{-0.9}$	...	...
X2	*XMM-Newton*	0693760401	2013 Nov 25	114 ± 3	419.712 ± 0.008	$0.2^{+3.4}_{-2.8}$
X3	*XMM-Newton*	0748390901	2014 Dec 10	284 ± 5	418.390 ± 0.008	$-0.5^{+3.0}_{-2.5}$
XN1	*XMM-Newton*, *NuSTAR*	0781800101, 80201010002	2016 May 20	519 ± 7	416.9513 ± 0.0017	−0.02 ± 0.16

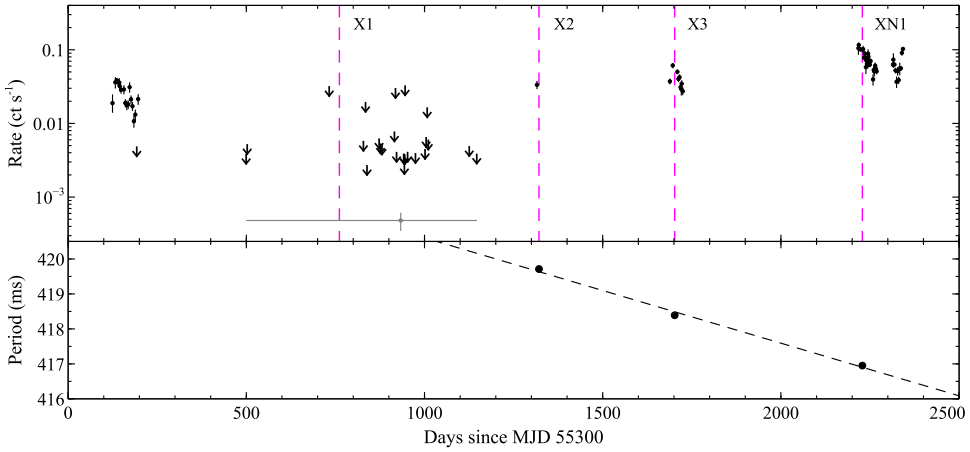

Figure 1. Top: long-term 0.3–10 keV *Swift* XRT light curve of P13 (1d bins), extracted with the standard *Swift* pipeline (Evans et al. 2009). The timing of the *XMM-Newton* only (X1–3) and *XMM-Newton*+*NuSTAR* (XN1) observations are indicated with the dashed magenta lines. While the source spends a lot of time in a bright state, during which it exhibits ULX luminosities ($L > 2 \times 10^{39}$ erg s^{-1}), during 2011 and 2012 it also exhibited an extended low flux period ($L < 10^{38}$ erg s^{-1}) indicated by the upper limits for individual observations spanning MJD ≈ 55800–56400 (see Motch et al. 2014). Stacking all the *Swift* observations during this period leads to a weak detection, shown in gray, >2 orders of magnitude fainter than the peak flux. Bottom: time evolution of the pulse period for the observations bright enough for pulsations to be detectable (X2, X3, and XN1). The dashed line shows a linear regression through these data.

we also analyze three archival *XMM-Newton* observations. Details of these observations are given in Table 1, and we show them in the context of the long-term behavior of P13 in Figure 1.

2.1. NuSTAR

The *NuSTAR* data were reduced using the standard pipeline, `nupipeline`, provided in the *NuSTAR* Data Analysis Software (v1.6.0), with standard filtering and *NuSTAR* CALDB v20160824. Source products were extracted from circular regions of radius 70″ for both focal plane modules (FPMA/B) using `nuprodcuts`, with background measured from large regions on the same detectors as P13. In addition to the standard "science" data, we maximize the signal-to-noise (S/N) by including the "spacecraft science" data following the procedure outlined in Walton et al. (2016). This increased the total good exposure time by ≈10%. Light curves were extracted in the 3–78 keV energy band with a maximal resolution of 0.1 s.

2.2. XMM-Newton

The *XMM-Newton* data were reduced with the *XMM-Newton* Science Analysis System (v15.0.0), following the standard prescription.[10] Owing to its superior time resolution of 73.4 ms, in this work we only consider data from the EPIC-pn detector (Strüder et al. 2001). The raw data files were cleaned using `epchain`. Source products were generally extracted from circular regions of radius ≈40″ (the exception being OBSID 0693760101, during which the source was extremely faint and a radius of 20″ was used) and the background measured from larger, source-free areas on the same CCD. As recommended, we only use single-double patterned events.

[10] http://xmm.esac.esa.int/

3. ANALYSIS

We calculate the power spectral density (PSD) for the 2016 *XMM-Newton* and *NuSTAR* light curves over a broad frequency range, starting at 1.24 (*XMM-Newton*) and 0.3 mHz (*NuSTAR*) up to their respective Nyquist frequencies (6.812 and 5 Hz, for *XMM-Newton* and *NuSTAR*). In both PSDs, a strong periodic signal is evident around ≈2.4 Hz, consistent between all instruments, at a significance $\gg 5\sigma$ assuming to white noise (Figure 2, left). The *NuSTAR* PSD is influenced by the variable dead time around 2.5 ms (Bachetti et al. 2015). However, the periodic signal is still significantly detected above this noise term.

To improve the period determination and search for a possible change in period ($\dot{P}$), we ran an accelerated epoch folding search (Leahy et al. 1983). We searched periods in a range of ±20 μs around the respective peaks in the PSDs. We searched a range of $\pm 1.5 \times 10^{-10}$ s s^{-1} around 0 for $\dot{P}$ (Figure 2, right). We sampled P and $\dot{P}$ on a grid of 200 values each, and used 12 phase bins for the pulse profiles.

Due to their long duration (≈200 ks), the *NuSTAR* data provide the strongest constraint on the pulse period, and we find $P = 416.951 \pm 0.002$ ms and $\dot{P} =$

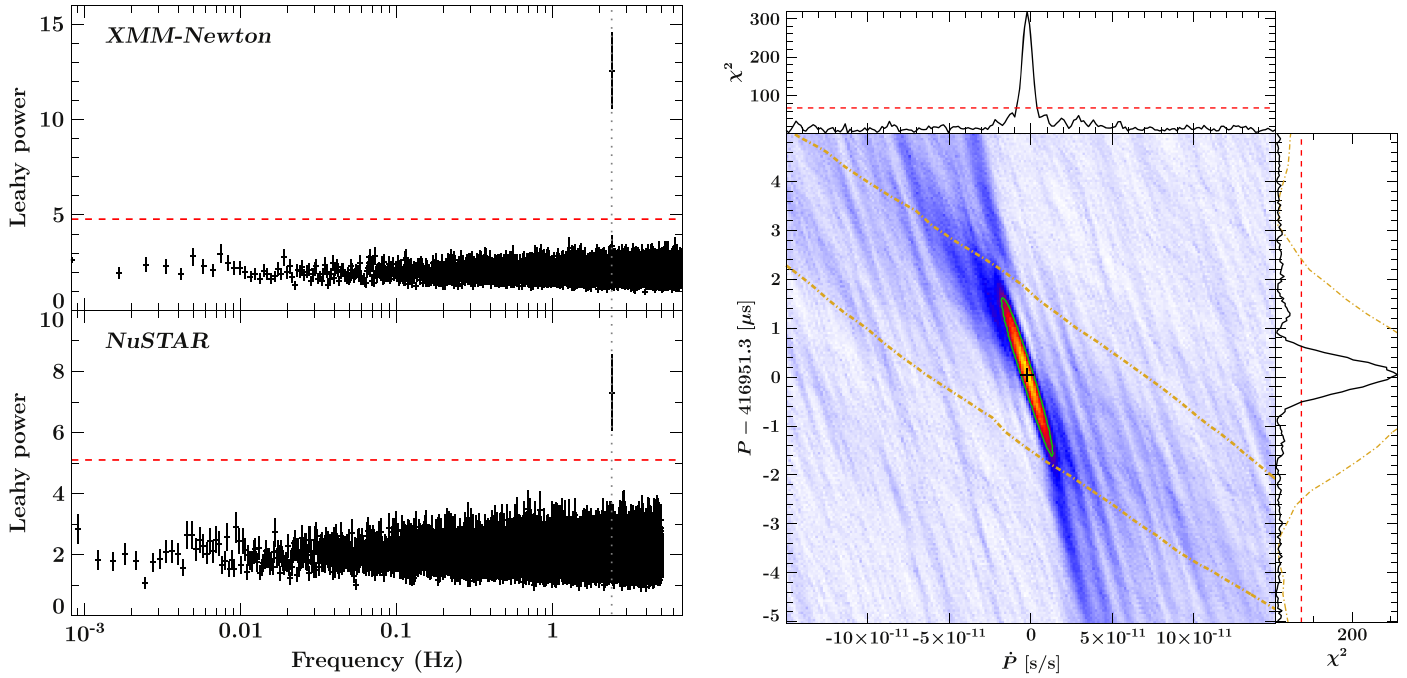

Figure 2. Left: PSD of the 2016 *XMM-Newton* EPIC-pn (0.3–10 keV; top) and *NuSTAR* FPMA (3–78 keV; bottom) data between 0.00124 and 6.812 Hz. The red dashed line shows the 5σ detection limit assuming white noise and accounting for the number of trials (8192 for *XMM-Newton* and 16,384 for *NuSTAR*; van der Klis 1989). Each bin is averaged over 39 and 34 independent PSDs for *XMM-Newton* and *NuSTAR*, respectively. The gray dotted line marks 2.398 Hz, at which a significant peak is seen in both PSDs. Right: result of the accelerated search of the *NuSTAR* data, showing the χ^2 values color-coded in the P–$\dot{P}$ plane. The green contour line shows the estimate uncertainty following the FWHM line. The top and right panels are cuts along the respective axes through the best-fit values. The red dashed lines in these panels indicate the 10^{-5} false detection probability. The brown dotted–dashed lines show the results for the 2016 *XMM-Newton* data.

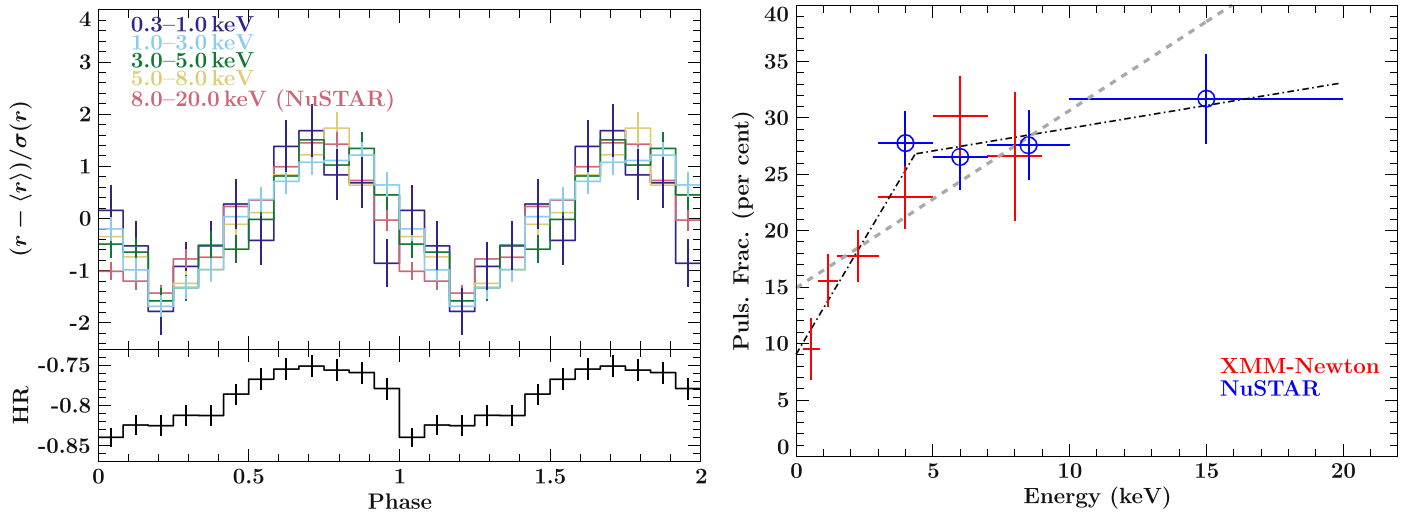

Figure 3. Top left: energy-resolved pulse profiles in the 0.3–1.0, 1–3, 3–5, and 5–8 keV bands of *XMM-Newton* and the 8–20 keV band of *NuSTAR*. The profiles are normalized by subtracting the average rate $\langle r \rangle$ and dividing by their respective standard deviations $\sigma(r)$. Bottom left: hardness ratio between the *XMM-Newton* 0.3–1 keV (S) and the *NuSTAR* 8–20 keV (H) band, defined as HR = (H-S)/(H+S). Right: pulsed fraction as a function of energy in *XMM-Newton* (red) and *NuSTAR* (blue) for a pulse profile with 10 phase bins. The gray dashed line gives the best-fit linear fit, while the dotted–dashed black line allows for a break in slope around 4.5 keV.

$(-0.2 \pm 1.6) \times 10^{-11}$ s s^{-1}. The uncertainties are estimated from the FWHM contours of the χ^2 landscape (Figure 2, right; i.e., they account for the degeneracy between P and $\dot{P}$). We confirmed the values of P and $\dot{P}$ through phase connection by separately folding the data of the first 50 ks and last 50 ks of the *NuSTAR* data and making sure no phase shift was evident.

Following this detection, we also examined the three archival *XMM-Newton* observations available. Unfortunately, the source was too faint during the 2012 observation to perform a meaningful pulse search. However, we find significant signals in the PSDs at ≈2.4 Hz in the 2013 and 2014 data. This is the only signal that is significantly detected in all calculated PSDs.

The measured values for P and $\dot{P}$ are given in Table 1 and the evolution in P as a function of time is shown in Figure 1. While the $\dot{P}$ measurements for the individual epochs are all consistent with zero, over the last three years an almost linear spin-up trend is visible, with $\dot{P} = (-3.486 \pm 0.003) \times 10^{-11}$ s s^{-1}.

The 2016 data are the only available broadband data for P13, and we use these data to calculate energy-resolved pulse profiles between 0.3 and 20 keV from the combined FPMA and FPMB events. These are shown for five energy bands in Figure 3 (left). The pulse profile is remarkably stable and sinusoidal as a function of energy and agrees well between the *XMM-Newton* and *NuSTAR* energy bands.

The pulsed fraction, however, changes significantly as a function of energy (Figure 3, right). The pulsed fraction PF(E) is calculated as

$$\mathrm{PF}(E) = \frac{\max(p(E)) - \min(p(E))}{\max(p(E)) + \min(p(E))}$$

where $p(E)$ is the energy-dependent pulse profile. The pulsed fraction increases from ≈8% in the 0.3–0.8 keV band to ≈30% in the 10–20 keV band, rising steeply before flattening out around 5 keV. A simple linear slope provides a statistically unacceptable description of the data; however, allowing for a break in slope around 4.5 keV describes the data very well (with an improvement in $\chi^2 > 10$ for one additional free parameter). The data can be similarly well described by a power law of the form E^{α} with an index of $\alpha \approx 0.3$.

The strong energy dependence of the pulsed fraction leads to significant spectral changes over the pulse phase (Figure 3, left). Here, the hardness ratio between the *NuSTAR* 8–20 keV and the *XMM-Newton* 0.3–1 keV band is shown. The spectrum is clearly softer during the low phase of the profile and hardens during the peak. A full spectral analysis of these data will be presented in a future work (D. J. Walton et al. 2016, in preparation).

Standard ULX continuum models (e.g., Bachetti et al. 2013; Rana et al. 2015; Walton et al. 2015) describe the data well and give an average 0.3–30 keV flux (which dominates the bolometric emission) of $(6.7 \pm 0.1) \times 10^{-12}$ erg cm^{-2} s^{-1}. This corresponds to an apparent X-ray luminosity of $\approx 10^{40}$ erg s^{-1} for the NGC 7793 distance of 3.6 Mpc (Tully et al. 2016). Scaling this to the average *Swift*/XRT count rate observed during 2013–2016 implies an average X-ray luminosity of $\approx 7 \times 10^{39}$ erg s^{-1} for this period. Note that we give the 0.3–10 keV flux in Table 1, for comparison with the *XMM-Newton*-only data sets.

4. DISCUSSION

Our timing study of NGC 7793 P13 using *XMM-Newton* and *NuSTAR* revealed pulsations with a period of ≈418 ms. This unambiguously identifies the compact object in the system as a neutron star. We find the pulse period in three separate epochs in 2013, 2014, and 2016. The source shows a significant average spin-up of $\approx 3.5 \times 10^{-11}$ s s^{-1} over the course of the past three years (Figure 1).

The remarkable discovery that M82 X-2, a ULX reaching apparent luminosities of $L_X \approx 2 \times 10^{40}$ erg s^{-1}, is powered by an accreting neutron star (Bachetti et al. 2014) naturally leads to the expectation of a larger population of ULX neutron stars (Mushtukov et al. 2015; Shao & Li 2015). However, prior to this work (and the simultaneous discovery of Israel et al. 2016), no other examples of such systems have been confirmed (Doroshenko et al. 2015). The detection of X-ray pulsations from P13 implies that neutron star accretors could play a significant role in terms of ULX demographics.

4.1. The P13 Binary System

The identification of the compact object as a neutron star confirms the basic conclusion of Motch et al. (2014) that P13 hosts a normal stellar remnant. The formal mass range for the accretor of 3–15 $M_{\odot}$ presented in that work explicitly assumes a BH accretor. If we allow also for a neutron star accretor, their constraint would presumably become an upper limit of $<15\,M_{\odot}$, consistent with the neutron star mass regime.

Motch et al. (2014) interpret the 64 day optical period as the orbital period and give best-fit radial velocity amplitudes between $K = 120$ and 290 km s^{-1} for the compact object. Even for a radial velocity as low as $K = 120$ km s^{-1}, this could result in a $\dot{P}$ over the long *NuSTAR* observation as large as 2.5×10^{-10} s s^{-1}, due to the Doppler effect of the orbital motion. We rule out a $\dot{P}$ of that magnitude from *NuSTAR* timing. However, the observable $\dot{P}$ vanishes close to superior and inferior conjunction. To reconcile the very small measured $\dot{P}$ with the orbital solution, our observation therefore has to have taken place close to one of the conjunctions. As we do not know the exact orbital phase of the observation, due to possible drifts with the potential ≈7 year super-orbital period (Motch et al. 2014), a more precise prediction of the expected $\dot{P}$ is currently not possible.

It is still interesting to speculate whether the origin of the observed 64 day period could be super-orbital instead of orbital as this would naturally explain the lack of observed $\dot{P}$. The period is similar to the ≈62 day period seen from M82 X-1 or X-2 (Kaaret & Feng 2007). It is most likely associated with X-2 (Qiu et al. 2015), and if so must be super-orbital. Motch et al. (2014) suggest that the period in P13 is orbital, as it is also seen in the radial velocity of He II. However, they note that the He II emission cannot arise in the stellar companion, as it is shifted in phase compared to the photometric period. Instead, the variations in He II could be related to super-orbital precession of the outer disk. A super-orbital nature would also explain the drifts of the photometric maxima observed by Motch et al. (2014). In this case, the orbital period would be much shorter, and the lack of $\dot{P}$ in any of the individual X-ray observations would imply that we view the source close to face-on.

As stated by Motch et al. (2014), the high luminosity rules out a purely wind-fed system. To sustain its luminosity, a mass accretion rate around $10^{-7}\,M_{\odot}$ yr^{-1} is required, which is comparable to the 4π mass-loss rates of B-stars (Vink et al. 2000). While wind clumping can locally increase the density and influence the estimated mass-loss rate (see, e.g., Oskinova et al. 2006), wind-fed systems can only capture a small fraction of that mass, even when allowing for an accretion stream. It is therefore likely that the companion is filling its Roche lobe (radiative or atmospheric; Podsiadlowski et al. 2002; Fragos et al. 2015), which distinguishes P13 from otherwise similar Galactic systems like Vela X-1 (see Fürst et al. 2010 and references therein).

4.2. Properties of the Neutron Star

In the standard disk accretion scenario as described by Ghosh & Lamb (1979; see also Dall'Osso et al. 2015), we can estimate the magnetic field from the change in pulse period:

$$-\dot{P} = 5.2 \times 10^{-10} {\mu_{30}}^{2/7} n(\omega_s, \mu_{30}) (P {L_{37}}^{3/7})^2 \text{ s s}^{-1} \quad (1)$$

assuming a neutron star mass of 1.4 $M_{\odot}$ and a radius of 10 km. Here, μ_{30} is the magnetic moment in units of 10^{30} G cm^{-3} and

L_{37} is the luminosity in units of 10^{37} erg s^{-1}. The dimensionless accretion torque $n(\omega_s, \mu_{30})$ depends only weakly on the magnetic field, and can be approximated analytically for small values of the fastness parameter ω_s (Ghosh & Lamb 1979). For the relatively high spin of P13, this results in values of $n(\omega_s, \mu_{30}) \ll 1$. From this equation we estimate the surface magnetic field strength of P13 to be $B \approx 1.5 \times 10^{12}$ G.

A field of the order of 10^{12} G is in the same range as expected in Galactic neutron stars, for example, as measured through cyclotron resonant scattering features (CRSFs; see, e.g., Caballero & Wilms 2012; Fürst et al. 2014, 2015; Staubert et al. 2014). We note that the observed changes in P seen between the different epochs cannot be explained by Doppler shifts due to the proposed 64 day orbit, as this effect is orders of magnitude smaller than observed.

From Equation (1) we expect a faster spin-up at higher luminosities. There is weak evidence that the average flux has been increasing over the course of the last three years, so we would therefore expect a higher spin-up in the 2016 observation than in 2013. Within each observation, the 2013 and 2014 *XMM-Newton* data are not sensitive to these small values of $\dot{P}$. The long-term $\dot{P}$, however, is higher than the one measured in 2016, indicating P13 was either even brighter during the gaps in the XRT coverage, potentially reaching apparent luminosities similar to M82 X-2, or that there are additional effects that influence the accretion torque.

4.2.1. Propeller Effect

Direct accretion can only take place if the corotation radius, $r_{\rm co}$, is outside the magnetospheric radius, r_m. The magnetospheric radius for spherical accretion can be calculated as (Cui 1997):

$$r_m = 2.7 \times 10^8 {L_{37}}^{-2/7} {B_{12}}^{4/7} \text{ cm}, \quad (2)$$

where B_{12} is the magnetic field in units of 10^{12} G. This is also a good approximation for the magnetospheric radius of an accretion disk if the magnetic field threads the disk completely (Wang 1996). We find that the corotation radius is about a factor of 2 larger than r_m for $B_{12} = 1.5$.

This relatively small difference between the radii implies that a drop in luminosity of only a factor of $\approx$10 ($r_m \propto L_{37}^{-2/7}$), related to natural fluctuations in the accretion rate, would therefore push P13 into the propeller regime, where $r_m > r_{\rm co}$. This would then truncate the disk at large radii, dramatically reducing the accretion rate even further and suppressing the X-ray flux (Cui 1997; Tsygankov et al. 2016), potentially explaining the very low luminosities observed before 2013.

The propeller effect has also been proposed by Dall'Osso et al. (2015) to explain the similarly large observed changes in luminosity and transitions between low and high states seen in M82 X-2 (Brightman et al. 2016). Such variability could therefore potentially be an indicator of a ULX pulsar and provide another avenue for identifying these systems.

4.2.2. Intrinsic Luminosity

Assuming isotropy, we measure a luminosity of $L_{\rm X} \approx 10^{40}$ erg s^{-1}, which is a factor of $\approx$50 above the spherical Eddington limit for a neutron star. One way in which the observed flux could be reconciled with the Eddington limit is if the emission is strongly beamed. However, this would obviously require an overall beaming factor of $\approx 1/50$. Such a tightly collimated beam should result in a narrow, strongly peaked pulse profile, which is clearly at odds with the smooth, sinusoidal pulse profile we observe. The pulse profiles of M82 X-2 and P13 are very similar in this respect.

This leads to a major uncertainty in the degree to which collimation and beaming contribute to the observed fluxes of ULX pulsars and how the magnetic field is configured. For example for M82 X-2, different analyses provide strongly different estimates for the magnetic field strength, ranging over 10^9–10^{14} G (Dall'Osso et al. 2015; Ekşi et al. 2015; Kluźniak & Lasota 2015; Mushtukov et al. 2015; Dall'Osso et al. 2016; King & Lasota 2016). So far, no model as been put forward that self-consistently reconciles the observed high luminosity, sinusoidal pulse profile, and high spin-up torque of the two known ULX pulsars.

Mushtukov et al. (2015), for example, attempt to estimate the maximum luminosity from the accretion column as a function of B-field. For $B_{12} = 1.5$, their calculations imply a maximum luminosity of $\approx 5 \times 10^{38}$ erg s^{-1}, which is still a factor of $\approx$20 below our measurement. The required beaming in this mode would still likely be at odds with the observed pulse profile. A better understanding of collimation and beaming in super-Eddington neutron stars is clearly necessary to link intrinsic and observed, isotropic luminosities in these systems, and more robustly constrain their magnetic fields.

5. CONCLUSIONS

We detected coherent X-ray pulsations from the ULX NGC 7793 P13, making this only the second confirmed ULX pulsar after M82 X-2 (Bachetti et al. 2014). Its properties seem to be in line with a high-luminosity extension of known Galactic neutron star binaries. Between observations in 2013 and 2016 we see a significant spin-up from which we estimate the magnetic field strength to be $\approx 1.5 \times 10^{12}$ G, typical of Galactic systems. Continued monitoring of the pulse period evolution of this remarkable source will be of particular value and help us understand if high variability is a tell-tale sign of super-Eddington neutron stars.

We would like the thank the referee for the helpful comments. M.J.M. acknowledges support from an STFC Ernest Rutherford fellowship, A.C.F. acknowledges support from ERC Advanced Grant 340442, and D.B. acknowledges financial support from the French Space Agency (CNES). This research has made use of data obtained with *NuSTAR*, a project led by Caltech, funded by NASA and managed by NASA/JPL, and has utilized the `nustardas` software package, jointly developed by the ASDC (Italy) and Caltech (USA). This research has also made use of data obtained with *XMM-Newton*, an ESA science mission with instruments and contributions directly funded by ESA Member States. This work made use of data supplied by the UK Swift Science Data Centre at the University of Leicester, and also made use of the XRT Data Analysis Software (XRTDAS) developed under the responsibility of the ASI Science Data Center (ASDC), Italy. This research has made use of a collection of ISIS functions (ISISscripts) provided by ECAP/Remeis observatory and MIT (http://www.sternwarte.uni-erlangen.de/isis/).

Facilities: NuSTAR, XMM, *Swift*.

REFERENCES

Bachetti, M., Harrison, F. A., Cook, R., et al. 2015, ApJ, 800, 109
Bachetti, M., Harrison, F. A., Walton, D. J., et al. 2014, Natur, 514, 202
Bachetti, M., Rana, V., Walton, D. J., et al. 2013, ApJ, 778, 163
Basko, M. M., & Sunyaev, R. A. 1976, MNRAS, 175, 395
Brightman, M., Harrison, F., Walton, D. J., et al. 2016, ApJ, 816, 60
Caballero, I., & Wilms, J. 2012, MmSAI, 83, 230
Coe, M. J., Burnell, S. J. B., Engel, A. R., et al. 1981, MNRAS, 197, 247
Cui, W. 1997, ApJL, 482, L163
Dall'Osso, S., Perna, R., Papitto, A., et al. 2016, MNRAS, 457, 3076
Dall'Osso, S., Perna, R., & Stella, L. 2015, MNRAS, 449, 2144
Doroshenko, V., Santangelo, A., & Ducci, L. 2015, A&A, 579, A22
Ekşi, K. Y., Andaçİ, C., Çıkıntoğlu, S., et al. 2015, MNRAS, 448, L40
Evans, P. A., Beardmore, A. P., Page, K. L., et al. 2009, MNRAS, 397, 1177
Fragos, T., Linden, T., Kalogera, V., & Sklias, P. 2015, ApJL, 802, L5
Fürst, F., Kreykenbohm, I., Pottschmidt, K., et al. 2010, A&A, 519, A37
Fürst, F., Pottschmidt, K., Miyasaka, H., et al. 2015, ApJL, 806, L24
Fürst, F., Pottschmidt, K., Wilms, J., et al. 2014, ApJL, 784, L40
Gehrels, N., Chincarini, G., Giommi, P., et al. 2004, ApJ, 611, 1005
Ghosh, P., & Lamb, F. K. 1979, ApJ, 232, 259
Harrison, F. A., Craig, W., Christensen, F., et al. 2013, ApJ, 770, 103
Herold, H. 1979, PhRvD, 19, 2868
Israel, G. L., Papitto, A., Esposito, P., et al. 2016, MNRAS, submitted (arXiv:1609.06538)
Jansen, F., Lumb, D., Altieri, B., et al. 2001, A&A, 365, L1
Kaaret, P., & Feng, H. 2007, ApJ, 669, 106
King, A., & Lasota, J. P. 2016, MNRAS, 458, L10
Kluźniak, W., & Lasota, J. P. 2015, MNRAS, 448, L43
Leahy, D. A., Elsner, R. F., & Weisskopf, M. C. 1983, ApJ, 272, 256
Middleton, M. J., Heil, L., Pintore, F., et al. 2015, MNRAS, 447, 3243
Miller, J. M., Raymond, J., Fabian, A. C., et al. 2004, ApJ, 601, 450
Motch, C., Pakull, M. W., Grisé, F., & Soria, R. 2011, AN, 332, 367
Motch, C., Pakull, M. W., Soria, R., et al. 2014, Natur, 514, 198
Mushtukov, A. A., Suleimanov, V. F., Tsygankov, S. S., & Poutanen, J. 2015, MNRAS, 454, 2539
Oskinova, L. M., Feldmeier, A., & Hamann, W. R. 2006, MNRAS, 372, 313
Podsiadlowski, P., Rappaport, S., & Pfahl, E. D. 2002, ApJ, 565, 1107
Poutanen, J., Lipunova, G., Fabrika, S., et al. 2007, MNRAS, 377, 1187
Qiu, Y., Liu, J., Guo, J., & Wang, J. 2015, ApJL, 809, L28
Rana, V., Harrison, F. A., Bachetti, M., et al. 2015, ApJ, 799, 121
Read, A. M., & Pietsch, W. 1999, A&A, 341, 8
Shao, Y., & Li, X. D. 2015, ApJ, 802, 131
Staubert, R., Klochkov, D., Wilms, J., et al. 2014, A&A, 572, A119
Strüder, L., Briel, U., Dennerl, K., et al. 2001, A&A, 365, L18
Tong, H. 2015, RAA, 15, 517
Tsygankov, S. S., Mushtukov, A. A., Suleimanov, V. F., & Poutanen, J. 2016, MNRAS, 457, 1101
Tully, R. B., Courtois, H. M., & Sorce, J. G. 2016, AJ, 152, 50
van der Klis, M. 1989, in NATO Advanced Science Institutes (ASI) Series C, Vol. 262, ed. H. Ögelman & E. P. J. van den Heuvel (New York: Kluwer Academic/Plenum), 27
Vink, J. S., de Koter, A., & Lamers, H. J. G. L. M. 2000, A&A, 362, 295
Walton, D. J., Harrison, F. A., Bachetti, M., et al. 2015, ApJ, 799, 122
Walton, D. J., Tomsick, J. A., Madsen, K. K., et al. 2016, ApJ, 826, 87
Wang, Y. M. 1996, ApJL, 465, L111